Solid Earth Discuss., 7, 1469–1515, 2015
www.solid-earth-discuss.net/7/1469/2015/
doi:10.5194/sed-7-1469-2015
© Author(s) 2015. CC Attribution 3.0 License.

Solid Earth Discussions
Open Access

This discussion paper is/has been under review for the journal Solid Earth (SE).
Please refer to the corresponding final paper in SE if available.

Magma mixing enhanced by bubble segregation

S. Wiesmaier[1,2], D. Morgavi[1,3], C. Renggli[4], D. Perugini[3], C. P. De Campos[1], K.-U. Hess[1], W. Ertel-Ingrisch[1], Y. Lavallée[5], and D. B. Dingwell[1]

[1]Ludwig-Maximilians-Universität München, Dept. of Earth and Environmental Sciences, Germany
[2]Department of Physics (Geology), GEOVOL, University of Las Palmas, Gran Canaria, Spain
[3]Department of Earth Sciences, University of Perugia, Perugia, Italy
[4]Research School of Earth Sciences, Australian National University, Canberra ACT 0200, Australia
[5]School of Environmental Sciences, University of Liverpool, Liverpool, UK

Received: 22 March 2015 – Accepted: 2 April 2015 – Published: 22 April 2015

Correspondence to: S. Wiesmaier (sebastian.wiesmaier@min.uni-muenchen.de)

Published by Copernicus Publications on behalf of the European Geosciences Union.

Abstract

That rising bubbles may significantly affect magma mixing paths has already been demon strated by analogue experiments. Here, for the first time, bubble-advection experiments are performed employing volcanic melts at magmatic temperatures. Cylinders of basaltic glass were placed below cylinders of rhyolite glass. Upon melting, interstitial air formed bubbles that rose into the rhyolite melt, thereby entraining tails of basaltic liquid. The formation of plume-like filaments of advected basalt within the rhyolite was characterized by microCT and subsequent high-resolution EMP analyses.

Melt entrainment by bubble ascent appears to be an efficient mechanism for mingling volcanic melts of highly contrasting compositions and properties. MicroCT imaging reveals bubbles trailing each other and multiple filaments coalescing into bigger ones. Rheological modelling of the filaments yields viscosities of up to 2 orders of magnitude lower than for the surrounding rhyolitic liquid. Such a viscosity contrast implies that bubbles rising successively are likely to follow this pathway of low resistance that previously ascending bubbles have generated. Filaments formed by multiple bubbles would thus experience episodic replenishment with mafic material. Inevitable implications for the concept of bubble advection in magma mixing include thereby both an acceleration of mixing because of decreased viscous resistance for bubbles inside filaments and non-conventional diffusion systematics because of intermittent supply of mafic material (instead of a single pulse) inside a material.

Inside the filaments, the mafic material was variably hybridised to andesitic through rhyolitic composition. Compositional profiles alone are ambiguous, however, to determine whether single or multiple bubbles were involved during formation of a filament. Statistical analysis, employing concentration variance as measure of homogenisation, demonstrates that also filaments appearing as single-bubble filaments are likely to have experienced multiple bubbles passages. In cases where bubbles have been essential for magma mixing, standard diffusion analysis may thus be inadequate for constraining timescales. However, data analysis employing concentration variance relaxation per-

SED
7, 1469–1515, 2015

mits the distinction of conventional single-pulse filaments from multiple bubble ascent advection in natural samples, demonstrating yet another powerful application of this novel petrological tool.

1 Introduction

Bubbles rising across fluid–fluid interfaces between two fluids may entrain and transport portions of one fluid into another (e.g., Thomas et al., 1993; Manga and Stone, 1995). As scenarios involving two fluids are the core feature of magma mixing, it is hypothesised that bubble ascent may be capable of intertwining two silicate melts and thus contribute to an efficient fluid mechanic mingling of two distinct magmas in nature.

Over the last two decades, magma mixing has received renewed attention in petrology (Wilcox, 1999). Traditionally, magma mixing served as an explanation, whenever a suite of igneous rocks yielded straight trends in chemical variation diagrams of major elements. Recently, however, magma mixing has been recognised to follow chaotic dynamics (Perugini and Poli, 2000; Perugini et al., 2003), which implies non-linear mixing behaviour due to diffusive fractionation of elements (Perugini and Poli, 2004; De Campos et al., 2010). Hybridisation is thus the result of multiple processes during the magmatic stage; fluid mechanical interaction of two magmas (mingling), and diffusion of elements across the interface of these two magmas (Perugini et al., 2012). These findings are fundamental for the concept of magma mixing, because they show that both, mechanic and diffusive equilibration, are necessary to achieve significant hybridisation. Chaotic mixing is thus not only a special case, but indeed generally characterises magma mixing by deconstructing it into two separate realms (mingling and diffusion), which may tackled separately by future studies. Notably, the degree of chaos in the generated filament structures may be variable.

The two-fold nature of chaotic mixing shows why different mingling processes predetermine the efficacy of magma mixing. Mingling may stretch and fold each liquid member, depending on its rheological properties, and thus results in increasingly com-

SED
7, 1469–1515, 2015

plex 3-D morphologies in the form of filaments and blobs (cf. Perugini et al., 2002). Because of the chaotic nature of mingling, de-mingling is precluded and physical mingling is irreversible. This irreversibility is enhanced by diffusion, which starts immediately in the presence of a compositional gradient at magmatic temperatures and smears the boundaries between two fluids. Without diffusion, mingling may be able to generate infinitesimally small filaments of two intertwined magmas, but chemically these filaments remain discrete. Diffusion is initiated at the moment of juxtapositioning of two magmas, as the system attempts to alleviate the perceived differences in chemical potential of the melt components. As the companion of magma mingling, diffusion drives a two-fluid system towards chemical homogenisation, but may or may not run to completion. Its efficacy however is highly dependent on the surface/volume ratio of the involved liquids, where high surface/volume ratios of the liquids (or complex 3-D morphologies) exponentially decrease the diffusive length scales (Perugini et al., 2003; De Campos et al., 2011). Because mingling generally increases the surface/volume ratio of the involved magmas, it follows that the efficacy of different mingling mechanisms affect the overall efficacy of magma mixing.

Magmas are mingled in nature through manifold mechanisms, which are mostly buoyancy-related. In detail, each of the mechanisms has its own dynamics. For example, during (i) conduit flow, the interface of two separate magmas may become instable and produce “streaky mixtures” of the two members. Although buoyancy-driven, conduit flow mixing is related to turbulence in the conduit, which may form at a lower Re number than expected for turbulence in isoviscous flow (Blake and Campbell, 1986). (ii) Vigorous convection in a magma reservoir, in turn, forms through strong T contrasts from transient mafic replenishment and may entrain, stretch and fold portions of mafic magma by viscous coupling (Huppert et al., 1983, 1984; Snyder and Tait, 1996). (iii) Double-diffusive convection depends on heat and molecular diffusivity, when both of “these two components make opposing contributions to the vertical density gradient” in a magma reservoir (Huppert and Turner, 1981). The implications of double-diffusive convection range from small-scale percolation of more felsic melts along the sidewall

SED
7, 1469–1515, 2015

of a reservoir, to catastrophic overturn when a replenishing mafic magma fractionates and becomes less dense than an overlying layer of magma. (iv) Forced intrusion implies a competent, felsic body of magma (mush), perhaps almost solidified but still hot, which is being intruded by a mafic dyke (Pallister et al., 1992; Izbekov et al., 2004). Simultaneous reheating of the felsic magma may lead to collapse of the dyke, because the surrounding felsic magma melts and loses strength to contain the magma into a rigid conduit. In such cases, highly variable quench textures in mafic enclaves may record the diminishing temperature contrast between mafic and felsic member (Wiesmaier et al., 2011).

In chemical engineering, bubble mixing is a long-recognised concept. Devices and set-ups exploiting the buoyancy force of gas in liquids have been employed for instance in medical and biochemical applications (e.g., Sánchez Mirón et al., 2004), fining of glass melts, waste waters treatment plants or blending of wines and spirits. In magma mixing, however, the role of bubbles has so far been limited to their density-diminishing effect on magma-bubble suspensions. Rapid exsolution of volatiles may reduce the bulk density of layers of basaltic magma to become less dense than an overlying layer of felsic magma (e.g., Tait et al., 1989; Ruprecht et al., 2008). The resulting instable configuration may then lead to a catastrophic overturn and eruption of an entire magma reservoir (e.g., Woods and Cowan, 2009). Several case studies have indicated a wider importance of bubbles in magma mixing. For instance, the vertical stratigraphy of the felsic member of the Bishop Tuff shows an inverse correlation of H_2O and CO_2, which may have been caused by the ascent of CO_2-rich bubbles into the felsic magma (Anderson et al., 1989). At Stromboli, intermingled deposits of yellow vesicle-rich pumice and degassed black scoria are related to paroxysmal episodes of increased CO_2 emissions (cf. Misiti et al., 2009).

Past experiments with analogue materials have clearly demonstrated the potential for rising gas bubbles to drag portions of one liquid into another (Thomas et al., 1993). Both, single bubbles and clusters of bubbles (as two-phase plumes), were observed to propagate portions of liquid of lower viscosity into an overlying liquid of higher viscosity.

SED
7, 1469–1515, 2015

Manga and Stone (1995) laid the fluid dynamical foundation of this problem; the low Reynolds number motion of bubbles or drops (generally: particles) that pass through fluid–fluid interfaces. Among other scenarios that study dealt with a single bubble rising from low-viscosity to high-viscosity fluid, thereby entraining parts of low-viscosity fluid into the upper high-viscosity one. Numerical constraints indicated the importance of viscosity contrasts between fluids and gas, along with interface Bond numbers. Analogue studies thus argue strongly in favour of bubble-driven mixing scenarios.

Here, we have reproduced for the first time (to the best of our knowledge) the mechanism of bubble advection, using volcanic melts at magmatic temperatures. Because mafic or hybrid filaments found in natural samples of igneous rocks are typically interpreted as result of convection-driven stretching and folding scenarios, we present a solution to distinguish such conventional filaments from filaments formed by bubbles.

2 Methodology

2.1 Glass preparation

The experiment has been carried out with two natural end-member compositions, basalt and rhyolite. Sample material was obtained in the form of blocks (> 30 cm) from the Bruneau–Jarbidge eruptive centre of the Snake River Plain-Yellowstone hotspot track. The rhyolite sample is from Unit V of the Cougar Point Tuff and the basalt sample from Mary's Creek (cf. Bonnichsen, 1982; Cathey and Nash, 2009). Samples of these units have been used in a previous study (cf. Morgavi et al., 2013). The basalt is of tholeiitic composition, and the rhyolite belongs to the subalkaline series (Table 1).

Both materials were freed from weathered surfaces and crushed. After TEMA milling, the basalt and rhyolite powders were melted and homogenised in a concentric cylinder viscometer (Dingwell, 1986) at 6 and 24 h respectively to ensure that the materials are exempt of crystals and gas bubbles. Both basalt and rhyolite melts were quenched in

SED
7, 1469–1515, 2015

air at room temperature. The glasses were cored from the crucibles and machined to cylinders that fit into a Pt crucible of 25 mm diameter.

2.2 Experimental set-up

At room temperature, a cylinder of Snake River Plain (SRP) rhyolite glass was placed above a cylinder of SRP basaltic glass in a Pt-crucible of 25 mm inner diameter (Fig. 1). This experimental charge was placed into a furnace at 1450 °C to remelt both glass cylinders. The heating rate was on the order of 5–15 K s^{-1} based on thermal diffusivity calculations. The target temperature was chosen to (a) keep the melts at supra-liquidus to avoid interference of particle-sized crystals and (b) to achieve a realistic viscosity for the rhyolite. Prior to the experiment, viscosity of the melts was measured by rotational viscometry and, at 1450° C, found to range around $10^{0.4}$ Pa s for the SRP basaltic melt and around 10^{4} Pa s for the SRP rhyolitic melt (Morgavi et al., 2013). As such, the relatively lower viscosity of our experimental rhyolite melt compared to that of a natural, H_2O-bearing rhyolite magma at depth ensures reasonable experimental runtimes, while maintaining fluid mechanical scalability.

Upon heating and melting, air trapped in the interstices between the glass cylinders and crucible walls formed bubbles, which rose into the rhyolite, thereby entraining portions of basaltic melt. Thin films of air were present underneath the basalt, in-between basalt and rhyolite, and in-between crucible wall and both glass cylinders. Bubbles were thus able to form below the melts as well as at the sidewalls, which ensured chaotic, unconstrained rising paths of bubbles. According to the ideal gas law, the increase in volume of the trapped air from 293 (20 °C) to 1723 K (1450 °C) was ca. six-fold. Oxygen fugacity was held constant in equilibrium with air at 1 bar. Bubbles rose from the basalt into the rhyolite above, traversing the compositional interface between these two (miscible and mixing) silicate melts and thereby propagating plumes of basaltic melt into the rhyolite (cf. Manga and Stone, 1995). Stokes' Law calculations indicated ca. 240 min for a bubble of radius 2 mm to rise through the rhyolite. At t = 180 min, the crucible was removed from the furnace and cooled in air to room temperature. The quench

SED
7, 1469–1515, 2015

rate is estimated to range around few degrees per second, similar to studies using comparable set-ups (e.g., Chevrel et al., 2015). The post-experimental glass assemblage was cored from the crucible to yield a sample cylinder of 20 mm diameter, which was subjected to further scrutiny. The resulting plume-like or column-like filaments that the advected basalt formed within the rhyolite (hereafter referred to as filaments) were characterized by microCT and subsequent high-resolution EMP analyses.

The current experiment is closely related to the numerical and analogue experimental approach by Manga and Stone (1995). Our system of rhyolitic and basaltic fluids and a free gas phase, air, is characterised following their notation; (i) the ratio of drop to lower fluid viscosity λ ranges around 2.35×10^{-5}, (ii) the ratio of upper to lower fluid viscosity γ is ca. 4×10^{3}, and (iii) a buoyancy parameter β, which approximates the buoyancy difference of the bubble translating from one liquid to another, is approximately 0.79; that is, the bubble in the rhyolite experiences 79 % of the buoyancy it had in the basalt. The *Re* number for a bubble of 4 mm radius rising through rhyolite ranges on the order of 1×10^{-9}. Bond numbers are $Bo_{bas} = 0.38$ for the bubble in basalt, and $Bo_{rhy} = 0.30$ for the bubble in rhyolite, using surface tension values for dry silicate melts from Bagdassarov et al. (2000). The Bond number for the interface of basaltic and rhyolitic melt is ∞ for lack of surface tension between miscible liquids (cf. Lacaze et al., 2010 and references therein). The present study extends the array of relevant fluid mechanical problems to low Re, low Bo and high log-Morton numbers (cf. Clift et al., 2005, Fig. 2.5 therein).

2.3 Micro Computed Tomography (MicroCT) analysis

MicroCT provided a non-destructive mean to qualitatively and quantitatively characterise the experimental products. MicroCT scanning was performed at IMETUM, Garching, Germany using a General Electric v|tome|x s© device equipped with a microfocal x-ray tube. Altogether 1000 scans were carried out, at 80 kV, 250 µA and an exposure time of 250 ms per scan. Each scan was conducted as average of 3 individual scans for noise reduction. The beam was moderated by a 0p3va filter for reduced

SED
7, 1469–1515, 2015

beam hardening. An effective voxel size of 50 µm was achieved. Subsequent reconstruction was conducted with VGStudio MAX©. The resulting stack of tiff-files was then converted to a volume file (.vox) using writeVOX, an auxiliary program of our custom made, MATLAB-based Tomoview software package. The vox-file was segmented in Tomoview and quantified for size parameters of subspherical bubbles.

2.4 Electron microprobe (EMP) analysis

After 3-D tomography, the cylinder of glass was sliced at different levels to obtain three sections of the experimental product. These discs of experimental glass were prepared as electron microprobe mounts and analysed for major element concentrations using a Cameca SX100 electron microprobe at LMU Munich. Measurements were carried out at 15 kV acceleration voltage and 20 nA beam current. To counter alkali loss, a defocused 10 µm beam was used for all elements. Standards used were; synthetic wollastonite (Ca, Si), periclase (Mg), hematite (Fe), corundum (Al), natural orthoclase (K), and albite (Na). Matrix correction was performed by PAP procedure (Pouchou and Pichoir, 1984). The precision was below 2.5 % for all analysed elements. Accuracy was tested by analysing MPI-DING standard glasses (e.g. Jochum et al., 2000) and is better than 3.0 % for the analysed elements.

2.5 Calculation of concentration variance

Concentration variance σ^2 represents a statistical measure for the degree of homogenisation of a filament and has been applied successfully in previous experimental studies on magma mixing (Morgavi et al., 2013a, b; Perugini et al., 2013). The calculation of σ^2 is given by

$$\sigma^2 = \frac{\sum_{i=1}^{N}(C_i - \mu_i)^2}{N} \quad (1)$$

SED
7, 1469–1515, 2015

where N is the number of samples, C_i is the concentration of element i, and μ is the mean composition. In order to provide readable numbers, we normalise concentration variance at time t to the initial variance at $t = 0$:

$$\sigma_n^2 = \frac{\sigma^2(C_i)_t}{\sigma^2(C_i)_{t=0}} \quad (2)$$

As a result, a value of 0 for σ^2 represents complete homogenisation, whereas a value of 1 equals completely separate end-members. For a correct statistical comparability of different transects and their values of concentration variance, we selected that the total number of data points of a transect should equal double the filament thickness. In some cases, compositional profiles have thus been complemented by rhyolite end-member data points to fulfil this requirement. Notably, this procedure has been used only for the calculation of concentration variance and all compositional data presented here are as measured from EMP analysis.

2.6 Model filaments

Model filaments were calculated to demonstrate the correlation of concentration variance with filament thickness in an ideal case. Ideal diffusion gradients have been modelled based on the thin-source problem and have been calculated using following equation:

$$C(x,t) = C_0 e^{-x^2/(4Dt)} \quad (3)$$

where x is the distance measured from the interface between end-members, C is the concentration of the diffusant, C_0 is the concentration of the diffusant at the surface ($x = 0$), D is the diffusivity, which is kept constant here, and t is time (after Eq. 37 in Zhang, 2010). Variables in the calculation of diffusion gradients were distance and diffusion times (10, 100, 1000 and 10 000 s). Filament thickness was varied by arbitrarily adding various amounts of end-member data points (basaltic and rhyolitic). The step length of

SED
7, 1469–1515, 2015

the model diffusion data was set to 15 µm (Fig. 2), comparable to the analytical profiles obtained by EMP in this study. Concentration variance was then calculated for each diffusion profile, and correlated with filament thickness.

2.7 Filament thickness

The thickness of experimental filaments has been determined for subsequent statistical analysis. In the final experimental charge, the original filament thickness is not preserved, because the onset of diffusion "smears out" the borders of filaments. Therefore, an arbitrary determination for the thickness of filaments has been devised to enable comparative analysis of filaments. The thickness of all filaments has been defined by the points of intermediate SiO_2 concentration between the measured maxima and minima of the respective transect (Fig. 2). As the main component of silicate melts, Si^{4+} represents a robust and reproducible proxy for filament thickness, not least for its relatively sluggish diffusion (Dingwell, 1990). According to this procedure, filament thicknesses of the nine EMP transects analysed here range from ca. 70 through 1650 µm. Potential errors from variable diffusivities of a single species in multi-component silicate melts are deemed insignificant due to the short run time of 180 min and the slow diffusivity of silica.

3 Results

3.1 MicroCT images

The reconstructed 3-D volume from the microCT scans shows compositional interaction between basalt and rhyolite driven by bubble motion (Fig. 3). Bubbles are observed arrested at various levels in the experimental charge. At the bottom of the rhyolite, which has been kept transparent for visibility in Fig. 3, we observe a horizon of ca. 50 bubbles (< 0.5 mm radius), some of them in the act of penetrating the rhyolite.

SED
7, 1469–1515, 2015

Their small radii (measured in the 3-D software) indicate very slow ascent speeds after Stokes' law, implying that their final vertical position is consistent with formation at the interface between basalt and rhyolite. Bubbles in the interior of the rhyolite are either with or without orange tail (filament). Bubbles without orange filament are interpreted to have entered the rhyolite from the side, without having encountered basaltic material. In turn, bubbles with a filament attached at their bottom must have been in contact to basaltic melt during their ascent. This shows that gas bubbles may advect volumes of low-viscosity silicate melt into a high-viscosity one. Several bubbles of up to 1.1 mm radius are embedded in a curved path of filaments. Because of the curvature of the filaments, the bubbles probably formed at the bottom between crucible wall and basalt, and traversed the circular basalt-rhyolite interface at its margin. The large bubble at the top broke the open surface of the rhyolite by the end of the experimental runtime and is interpreted as the result of coalescence of many smaller bubbles. Aspect ratios of bubbles suspended in rhyolite have been calculated. Only bubbles not in the process of coalescence and of enough distance to other bubbles or the interface have been considered for the measurement of aspect ratios. Measured bubbles (n = 8) were close to being equant, with ellipsoid radii deviating to a maximum of 36 vs. 33 % in a perfect sphere (Table 2).

The filaments in the 3-D volume have greyscale values intermediate to those of the basalt and the rhyolite glass. Since the attenuation value in radiographies represents the cumulative attenuation of all elements or ions in the scanned silicate melts, the greyscale values of the filaments (coloured orange in Fig. 3) suggest hybrid composition on first order. In cross section, this hybrid phase appears at the top in the form of a thick cylindrical filament attached to the bottom of the topmost bubble. About 5 mm deeper, the thick filament fans out into multiple filaments of several hundreds of micron thickness (this observation supports the interpretation that the top-most bubbles had coalesced from several bubbles). The multiple small filaments extend downwards from the main stem of the plume tail in curves, bending towards the crucible margin.

SED
7, 1469–1515, 2015

Some artefacts are observed in the 3-D volume. The basalt in yellow appears to feature a grainy texture, which has been caused by the fine segmentation needed to differentiate hybrid melt from basalt. The glass has been confirmed to be homogeneous in section. A second artefact is indicated by the orange voxels along the vertical edges of the 3-D cuboid. The original experimental shape was of cylindrical shape, but displayed a circumferential interference interpreted as beam hardening. To clarify the 3-D volume for visual inspection, the cuboid shape was chosen to free the sides of the sample from visual obstruction.

3.2 Composition of experimental glasses and diffusion profiles

The experimental glass has been sectioned at three different levels perpendicular to the long axis of the cylindric experimental charge. BSE images and the corresponding analytical profiles of these three levels are shown in Fig. 4. The uppermost level, SWM01, features a basaltic area of sub-spherical shape of ca. 2.5 mm diameter. The intermediate level SWM02 shows a convoluted, but coherent single filament. The lowest level SWM03 appears as three or four separate filaments of varying thickness. The single filament in sample SWM01 required one profile only (SWM01-01), whereas the more convoluted filament structures of SWM02 and SWM03 were characterised by four EMP profiles each (Fig. 4). The analytical profiles of each filament are grouped into three classes: bell-shaped, plateau-shaped and multi-peak/irregular shape.

3.2.1 Section SWM01

The transect across the sub-circular filament of SWM01-01 covers a distance of ca. 2800 µm. Diffusion profiles of all major elements are symmetric and plateau-shaped. On either side, ca. 500 µm of pristine rhyolite have been measured, before a transition towards more mafic composition. These gradients, one from either side, cover variable distances depending on the element measured and are between 100 and 400 µm long. The middle section of the analytical transect is relatively flat. There, the most

SED
7, 1469–1515, 2015

mafic composition of the profile is detected, although the composition is still clearly hybridised, and its classification borders the fields of andesite and trachy-andesite (Fig. 5).

3.2.2 Section SWM02

SWM02-01. The profile of SWM02-01 is sub-symmetrically bell-shaped for most major elements, but, compared with SWM01-01, shows a much smaller compositional span. The most "mafic" composition detected is low-SiO_2 rhyolite. Na_2O appears overlain by the analytical error and K_2O measurements exceed the concentration expected for the rhyolite.

SWM02-02. As other transects, this EMP transect started in glass of rhyolitic composition. However, the transect is asymmetric and recorded more mafic glass at the other end. This precluding certainty of having measured the most mafic composition in the filament. SWM02-02 is therefore excluded from further interpretation.

SWM02-03 shows two peaks in all element profiles. Probably, two separate filaments of either different thickness or different time of hybridisation are combined in the analysed filament. A useful estimation of diffusion rates is thus hindered in transect SWM02-03, which is consequently excluded from the interpretation of diffusion profiles.

SWM02-04. The diffusion profiles are bell-shaped, but of little amplitude. In the TAS diagram, all data points cluster very near the original composition of the end-member rhyolite. In such cases, the analytical error was significant in the variation of Na_2O, K_2O and TiO_2 concentrations, which affects the calculation of concentration variance values.

3.2.3 Section SWM03

SWM03-01. The profiles appear similar to SWM02-04 with very little variation and all data points group very near the original composition of the end-member rhyolite. Again,

SED
7, 1469–1515, 2015

the analytical error may be significant in the variation of Na_2O, K_2O and TiO_2 concentrations.

SWM03-02. Most profiles are sub-symmetrically bell-shaped, and span a compositional range of rhyolite to dacite/trachyte. Again, Na_2O data appears affected by the analytical error and K_2O measurements exceed the concentration expected for the rhyolite.

SWM03-03 shows sub-symmetrical bell-shaped profiles, which amount to rhyolitic to trachy-andesitic composition. Also here, the profile of Na_2O seems affected by the analytical error and K_2O data are higher than expected for the rhyolite.

SWM03-04 profiles appear bell-shaped, but, as for some of the previous transects, with very little compositional variation. In the TAS diagram, all data points group very near the original composition of the end-member rhyolite. The analytical error was significant in Na_2O, K_2O and TiO_2.

In summary, analytical transects may be grouped as follows (see Fig. 4); (a) bell-shaped (SWM02-01, SWM02-04, SWM03-02 and SWM03-03), (b) plateau-shaped (SWM01-01), and (c) multi-peak/irregular (SWM02-02, SWM02-03, SWM03-01 and SWM03-04). Common to all of the 9 analysed filaments is that the basaltic end-member is not preserved. Hybridisation was thus pervasive for all filaments.

3.3 Results of model filament calculation

In model filament calculations, concentration variance correlates systematically with filament thickness. In Fig. 6, each curve represents concentration variance vs. filament thickness at a specified diffusion time. Concentration variance, i.e. the degree to which filament of thickness x has equilibrated during this interval of diffusion, correlates non-linearly with filament thickness.

When end-member compositions, diffusion time and diffusivities are equal, thicker filaments are less homogenised, which increases the value of concentration variance (cf. Morgavi et al., 2013). At similar diffusion time, thinner filaments will have disproportionally lower values of σ^2 compared to thicker ones, i.e. thin filaments equilibrate

SED
7, 1469–1515, 2015

faster than thick ones. Curves of longer diffusion time show that this contrast between thick and thin filaments lessens with increasing diffusion time, although the overall non-linearity remains.

Along each curve, increasing the filament thickness causes the values of σ^2 to asymptotically approach unity, whereas in regions of small filament thickness the curves possess a relatively steep slope. This indicates a more pronounced difference in equilibration speed for small filaments, and the difference in degree of homogenisation between two filaments of "neighbouring" thickness becomes more pronounced the thinner both are.

The polynomial regression for concentration variance vs. filament thickness allows characterising the model of diffusive equilibration. All calculated regressions have $R^2 > 0.998$. The asymptotic nature of the regression curves implies that its 1st derivative approaches zero at infinite filament thickness. Comparison of regression curves for diffusion times of 10, 100, 1000 and 10 000 s. shows less sharp curvatures for longer diffusion times. The 2nd derivative as measure of curvature confirms this by showing much lower values for longer diffusion times. At short diffusion times of 10 s, for instance, the regression shows a sharp bend at ca. 500 µm filament thickness, implying that thicker filaments may hardly experience significant diffusive equilibration, whereas filaments of 500 µm or thinner will disproportionally equilibrate more at such short diffusion times. The non-linearity of the regression curves is thus evidence for an exponential decrease in equilibration time-scales with decreasing filament thickness.

3.4 Filament rheology

Here, we calculate viscosities of hybrid filaments based on compositions measured by EMP. The initial viscosity contrast of the pure end-member was a factor of 4×10^3 (cf. Morgavi et al., 2012). The compositional data of the filaments allows the constraining of the viscosity in their respective centremost points by employing the viscosity model of Giordano et al. (2008). Under the experimental conditions (1 atm, 1450 °C), the rhyolitic end-member possesses a calculated viscosity of ca. $10^{3.8}$ Pa s, compared

SED
7, 1469–1515, 2015

to a measured 10^4 Pa s. The most mafic composition of each individual filament varies strongly among filaments. As a result, the computed minimum viscosities across all filaments range between ca. $10^{1.5}$ and ca. $10^{3.5}$ Pa s. Viscosity contrasts between rhyolitic and hybrid melt thus range between a minimum factor of 3, to in excess of 2 orders of magnitude. Viscosity contrasts roughly correlate with filament thickness.

4 Interpretation and discussion

4.1 3-D images and continuum mechanical appraisal of the experimental sample

The imaging results from microCT reveal that multiple bubbles have risen through the rhyolite, dragging portions of basaltic melt upwards with them (see Fig. 3). These subvertical elongated filaments are hybridised, according to microCT attenuation values. Because several hybrid filaments merged into one thicker filament underneath the topmost bubble, bubbles appear to have exploited the same pathway repeatedly. The experimental set-up has thus generated two main modes of mass transport. Firstly, advection of basaltic into rhyolitic melt driven by the segregation of bubbles. Secondly, diffusion of ionic species across the boundary between basalt and rhyolite melts.

Several implications arise from comparison of our experiment to the numerical analysis of migration of drops through fluid-fluid interfaces (Manga and Stone, 1995). Based on numerical constraints, Manga and Stone (1995) suggested that the volume of entrained fluid decreases with increasing γ (ratio of upper to lower fluid viscosity). As our experiment constitutes a case of high γ (ca. 4×10^3), the entrained volume of basaltic melt should be low, perhaps insignificant. However, according to the microCT image, significant amounts of basaltic melt have been propagated, which either indicates that generally the amount of entrained fluid may approach a minimum of > 0 asymptotically, or the higher value of β (0.2 in the numerical solution vs. 0.79 in the experiment) causes a relatively higher buoyancy of the bubble in rhyolite to still permit significant

SED
7, 1469–1515, 2015

volumes of entrained melt. Bubbles are free of films of mafic or hybrid material around them, the gap thickness is consequently zero.

The time of penetration of a bubble into the upper layer, or breaking the interface between basaltic and rhyolitic melt, scales at a factor of approximately $1/(1+\lambda)$ of the ascent rate, where λ is the ratio of bubble to lower fluid viscosity (Rallison, 1984; Kojima et al., 1984). For our experiment, the large viscosity contrast of air and basaltic melt at 1723 K implies a λ of around 2.35×10^{-5}, meaning the ascent rate of bubbles would hardly be affected by the interface and bubbles essentially pass through with nearly no deceleration. This is consistent with Manga and Stone (1995, Fig. 8d therein, $\lambda = 10$), where the rise speed decreases continually upon entering the higher viscosity upper liquid, but potential interface effects in the form of a rise speed minimum are not detected.

Discrepancies between our experiment and the numerical treatment of Manga and Stone (1995) arise with respect to Bond numbers and surface tension. The surface tension of dry silicate melt against a free vapour phase is an order of magnitude higher than the surface tensions employed for the fluids in the analogue experiments of Manga and Stone (1995). In the present case, the bubble Bond number Bo_1 is closer to 1, or somewhat below, whereas Manga and Stone (1995) addressed problems of $Bo_1 > 5$. Smaller Bond numbers imply that bubble deformation in the rhyolite is limited, which, in turn, is consistent with the 3-D data obtained from the experimental charge; the measured aspect ratios of bubbles suspended in rhyolite are close to being equant.

In summary, bubble mixing efficiently works at viscosity contrasts of up to 4×10^3. We note that in nature viscosity contrasts may be lower, as the most extreme melt compositions were chosen for this experiment. A lower viscosity contrast would cause more yet more favourable conditions for bubble mixing. Specific to bubble mixing is that successive bubbles have each advected mafic material into the same filament. A filament may thus experience mafic recharge at irregular frequency. This gives rise to a complex diffusion scenario in which the starting composition may be replenished time and again, thus hindering the application of standard diffusion systematics. Addi-

SED
7, 1469–1515, 2015

tionally, later pulses of basalt, delivered by ascending bubbles, may have arrived at the top of the experimental column having experienced smaller degrees of hybridisation during ascent. Also the composition of the advected melt may therefore vary with time. As a result, not only the mode of advection is non-conventional (bubbles instead of inherent buoyancy or convection), but also the calculation of diffusion timescales must take into account, that additional mafic melt may or may not have been added to the filament at later stages.

4.2 Rheology of hybrid filaments

The compositional variations across the filaments imply a dynamic rate change for bubble mixing. The viscosity contrast from basalt to hybridised filament is smaller than from basalt to pristine rhyolitic melt. Figure 7 shows this "viscosity valley" in the interior of filaments compared to the surrounding rhyolite. Computing the log viscosities, the viscosity contrast at $t = 0$ was 4000 and at $t = 3$ h is reduced to ca. 32 for filament SWM01-01. This reduced viscosity contrast after 3 h runtime may strongly affect ascent velocities of bubbles that trail previously ascended bubbles.

It is important to note, however, that these fluid mechanic numbers are transient. Diffusion constantly aims to equilibrate compositional gradients, whilst new bubbles advect more mafic material, increase the chemical potential in the melt and therefore increase the disequilibrium. Thus, the numbers and the discussion provided here are essentially snapshots of a dynamic system. However, the qualitative notions hold fast. For any felsic melt, an intrusion by bubbles, which advects melt of more mafic composition, will imply a reduced viscosity in newly formed filaments.

The consequences of the presence of low viscosity filaments for bubble mixing are manifold. First of all, higher ascent velocities are expected for bubbles that rise within a filament, as Stokes' Law correlates linearly with viscosity. Therefore, at the calculated filament viscosity of ca. 32 Pa s (compared to 10 000 Pa s in the rhyolite), the terminal settling speed of a bubble may be up to 300 times faster in a hybrid filament than through pristine rhyolite. The reduced viscosity must therefore enhance the rate of bub-

SED
7, 1469–1515, 2015

ble ascent. Secondly, the ratio of viscosities of upper to lower fluid γ affect how much basaltic melt can be advected. According to Manga and Stone (1995), γ inversely correlates with the amount of lower fluid entrained into the upper liquid. For filament SWM01-01, γ changed from 4×10^3 down to 13, implying an increase in transported material. When a bubble enters a hybrid filament, it may thus be able to propagate larger amounts of basaltic liquid than upon entering pristine rhyolite. This affects the mixing rate once more, as more material per bubble is being advected. Thirdly, the buoyancy change β that the bubble experiences upon entering the upper fluid will be diminished. Calculation of β using the viscosity of the hybrid filaments implies a reduced buoyancy change (from 0.8 to 0.9), because the hybrid filament has a higher density than the surrounding rhyolite. The higher value of β implies lesser deceleration of the ascent speed caused by the viscosity contrast. Not only does the rise speed within the rhyolite increase, but also the rise speed through the basalt-rhyolite interface.

Bubble and streamline geometry will have additional effects on bubble mixing, although these cannot be directly observed from our experiment. Assuming a second bubble enters a hybrid filament possessing the same diameter as the first bubble. Streamline geometry indicates that the bubble may not only be affected by the filament's reduced viscosity, but also by the rhyolite's higher viscosity, because the bubble diameter will be several times wider than the filament. Assuming a second bubble of smaller diameter, the values of γ and β favour an accelerated ascent of the bubble, on one hand. On the other hand, this may be counterbalanced by less buoyancy of the smaller bubble and less amount of advected basaltic fluid. From this point of view, the enhanced efficacy of bubble advection by the formation of hybrid filaments may therefore be lower than indicated by the numerical parameters of this specific experiment.

The last point to consider is filament geometry. Filaments are widening due to addition of new mafic melt by each passing bubble. For example, the uppermost filament from our experiment shows visual evidence that it formed as many pulses of mafic melt, which probably caused the disproportionate thickness of this filament. The repeated advection of multiple basalt-propagating bubbles through a pathway very likely

SED
7, 1469–1515, 2015

causes a thickening of the filament, thus enhancing bubble advection by enlarging the diameter of the low-viscosity channel. Additionally, recurring bubble advection may create a network of hybrid filaments by coalescence of bubbles and merging filaments.

Continuum mechanics therefore indicate that bubble advection is enhanced threefold, once the first bubbles and filaments have risen through the rhyolite.

The reduced viscosity inside the filaments causes

1. increased ascent speed of subsequent bubbles,
2. more basaltic fluid to be entrained per bubble and
3. accelerated traversal of the bubble across the basalt-rhyolite interface.

The acceleration of the rate of mixing may in theory continue until filaments purely consist of mafic end-member, at which point the lowest possible viscosity is established inside the filament. By then a steady state would be reached and new mafic material advected at a constant rate per bubble and bubble size. Once the source reservoir of the mafic end-member is depleted of a free gas phase, mixing induced by bubbles must decelerate until more volatiles are exsolved or external volatile sources are tapped. Recent advances in the understanding of magmatic assimilation have hinted at the possibility of rapidly freeing large amounts of CO_2, when decomposition of carbonates is involved (e.g., Freda et al., 2008; Mollo et al., 2011). During assimilation of volatile-bearing rocks, the homogenisation of compositional gradients (mixing between assimilant and assimilate) may thus be significantly enhanced by bubble advection.

In nature, the process of bubble advection would thus accelerate with time. Once the first bubble has overcome the rheological threshold of the more felsic material, a filament of more mafic, less viscous, material will be present within the felsic end-member. Subsequent bubbles may exploit this plume of mafic material as pathway and traverse the horizontal boundary between upper and lower liquid faster, rise faster within the upper liquid and advect more material than the first bubbles.

SED
7, 1469–1515, 2015

4.3 Comparison of model filaments with bubble advection filaments

The above results show that magmatic filaments may form by multiple bubbles rising through the same filament. When considering that each rising bubble represents a new pulse of mafic material, this implies that an associated filament formed from such multiple pulses of bubble ascent follows rather distinctive diffusional equilibration dynamics. Instead of a single pulse of melt, which progressively equilibrates, multi-pulse filaments are irregularly replenished, thereby resetting the diffusion of the previous pulse by providing pristine end-member material. Multi-pulse filaments may thus significantly deviate in their diffusional behaviour from single pulse filaments. This is important because the calculation of magmatic time-scales based on diffusion gradients has commonly been based on a single pulse origin of magmatic filaments, bar other options recognized so far. It is thus vital to be able to distinguish single- from multi-pulse filaments in natural samples.

The characteristics of our experimental charge are advantageous for distinction of single and multi-pulse filaments, as it is comparable to natural samples in key aspects. First of all, bubbles were allowed to rise in uncontrolled fashion. The resulting filaments are thus a result of the conditions in-situ within the experimental charge, and mainly controlled through the parameters buoyancy, surface tension and rheology. Secondly, the time evolution of the experiment is uncontrolled except for the total runtime. Due to the experimental set-up in a platinum crucible at high temperature, direct observations throughout the experiment were inhibited. Therefore, the motion of individual bubbles can only retrospectively be constrained by position and dimension. However, both, time evolution and locii of bubbles are necessarily unconstrained in a natural sample as well. Our experimental design thus mimics natural samples in these aspects, while on the other hand has the advantage that pressure, temperature and initial end-member compositions are known. This allows us to constrain the origin of the filaments generated during the experiment to a further degree than possible in natural samples.

SED
7, 1469–1515, 2015

4.3.1 Compositional profiles of filaments indicate their formation mechanism

The shape of compositional profiles obtained from filaments allows a qualitative estimation of filament formation. Three different shapes of compositional profiles have been observed: (a) multi-peak or irregularly shaped, (b) plateau-shaped and (c) bell-shaped (see Fig. 4).

1. Multi-peak or irregular shapes of analytical profiles are not explicable by standard diffusion models and thus have most likely been affected by multiple bubbles having risen through (see Fig. 4b).

2. Plateau-shaped profiles (see Fig. 4a), in turn, permit both possibilities, single and multiple pulse origin. The distinction of plateau-shaped profiles lies in the preservation of the original mafic end-member. If the plateau of the profile is equal to the original end-member composition, then standard diffusion theory applies, and a single-pulse origin is probable. Should the plateau lie at a hybrid concentration between both end-members, it cannot be the result of a single-pulse that diffused partly into its surroundings. This is because in a single-pulse filament the centre can only be hybridised after the plateau has been obliterated by diffusion. In our experiment, filament SWM01-01 shows such a compositional profile that is both, shaped as plateau and of hybrid composition at its plateau. The profile must thus represent a composite structure of multiple filaments, and episodic replenishment of the filament with basaltic material has to be expected. Here, the multi-pulse origin of filament SWM01-01 is also confirmed by microCT imaging, which shows several bubble trails (filaments) converging to the final filament (see Fig. 3). We nevertheless discuss the compositional profiles at length, because 3-D imaging technology is not always available for sample scrutiny, but knowledge on the origin of filaments useful for interpretation of diffusion-related data. Additionally, the diffusional profile of SWM01-01 shows a slight gradient in the plateau itself, which may be a result of the replenishment (see Fig. 4a). Potentially, a first diffusion

SED
7, 1469–1515, 2015

gradient developed between first pulse of basalt and rhyolite, and a second one between second pulse basalt and hybridised (initial) basalt.

3. Bell-shaped profiles (see Fig. 4c) are ambiguous in the context of our experiment. On one hand, these analytical profiles approach a Gaussian distribution, presumably indicative of a single pulse origin. However, 3-D data also indicate a multi-pulse origin. As additional observation, the reduced viscosity of hybrid filaments compared to surrounding rhyolite indicates that they may act as chimneys of less viscous resistance, irrespective of their exact compositional profile.

The analysis of compositional profiles of the magmatic filaments from this experiment opens up an interesting question. May a filament have been produced by a single pulse of magma (in the case of this experiment, this would translate to a single bubble), or have multiple pulses been involved? This question is relevant for two reasons. First of all, the notion of multi-pulse filaments is quite uncommon in igneous petrology. Including the most recent works on magma mixing, magmatic filaments are perceived as one single pulse of magma by design. Even if a filament may be stretched and folded ad infinitum, it will never be replenished by fresh mafic magma. As a result of the present study, we observe the possibility that filaments, are falsely perceived as single pulses of magma. Secondly, when analytical profiles of filaments are used for the calculation of diffusional time-scales, these time-scales are commonly calculated with the tacit assumption that a single pulse of magma formed the filament in question. Application of conventional single-pulse diffusion systematics on a multi-pulse filament may yield erroneous results. We therefore propose the following method for distinction of single- and multi-pulse filaments.

4.3.2 Concentration variance vs. filament thickness

To distinguish single- from multi-pulse filaments, we devised a method to statistically distinguish filament origins based on EMP data. The statistical analysis attempted here provides a method for determining whether or not a set of filaments that feature bell-

SED
7, 1469–1515, 2015

shaped compositional profiles have a complex history of formation. Here, we therefore compare the values of concentration variance from our experimental filaments with theoretical values computed from ideal "model filaments" (see Sect. 2.6). The model filaments have been calculated with boundary conditions consistent with our experimental set-up; end-member compositions, temperature and diffusivities were kept constant. The model filaments have been computed as single pulse filaments, and thus characterise the diffusive equilibration of individual filaments under ideal conditions. For the comparison, only the experimental filaments showing bell-shaped analytical transects have been used in the following; transects SWM02-01, SMW-02-04, SWM03-02 and SWM03-03.

Figure 8 shows the correlation of concentration variance and filament thickness for the four bell-shaped filaments from the bubble mixing experiment. The regression curves of their concentration variance possesses the opposite orientation compared to the ideal data (downwards convex vs. upward convex), therefore the regression is fundamentally dissimilar to the regressions obtained from the model filaments (i.e. from "ideal behaviour"). This qualitative argument becomes more obvious when considering specific data points. For example, data points SWM03-01 and SWM02-04 are from filaments of different thickness but show very similar values of concentration variance with potassium (Fig. 8, second panel). This stands in contrast to the ideal behaviour of filaments, as the slope of the regression curves characterising ideal filaments requires different degrees of equilibration for filaments of different thickness. The argument is aggravated by the notion that SWM03-01 and SWM02-04 are relatively thin filaments ($< 100\,\mu m$), because for thin filaments the ideal regression curves possess the steepest slope. Any difference in equilibration, when filament thickness is the sole variable, should thus be most obvious in very thin filaments. This behaviour repeats itself through all major elements and indicates a formation mechanism different to single pulses of magma.

Even though all four filaments possess bell-shaped compositional profiles, multiple bubbles seem to have been involved in the formation of at least some of these fil-

SED
7, 1469–1515, 2015

aments, so that the overall correlation deviates from ideal conditions. This confirms the visual observations from 3-D microCT analysis, which indicated multiple thin filaments converging to larger ones. The statistical appraisal of diffusional equilibration thus provides a further constraint on the multiple-pulse origin of filaments generated by bubble advection. Bell-shaped compositional profiles of magmatic filaments thus have to be viewed with care and are not automatically indicative of a scenario of standard diffusional equilibration. As the exact mechanisms and conditions of formation are essentially unknown for any natural sample, magmatic filaments and their observed compositional patterns need to be tested for whether or not bubbles have played a role for magma mixing. Especially, since rheological factors strongly favour a multi-pulse origin of filaments during bubble mixing. Correlation of filament thickness and concentration variance thus represents a simple and straightforward tool to constrain the origin of a cohort of filaments from one sample.

4.4 Bubble mixing at variable temperature conditions

For our experiment, the furnace temperature was chosen to achieve a combination of feasible viscosity contrast, crystal-free melts and relatively short run time. We envisaged our experiment to approximate the fluid dynamic behaviour at no or little temperature contrast between two fluid magmas to avoid kinetics of thermal equilibration affecting the results. Notably, however, temperature contrasts between mafic and felsic magma may vary in nature, which merits the question whether or not a mechanism such as bubble mixing may be inhibited in nature by quenching of one magma against another.

Previous studies have indicated the potential for the formation of quench textures, or even quench horizons, when for instance a hot basaltic magma is juxtapositioned on a much cooler, felsic magma (e.g., Eichelberger, 1980). Such quench textures abound at the margin of mafic enclaves in many natural outcrops, and are the result of strong temperature contrast and short time-scales of interaction between mafic and felsic magma (e.g., Coombs et al., 2003). These time-scales are short, because steep tem-

SED
7, 1469–1515, 2015

perature gradients and small volume of individual enclaves cause the mafic enclave to rapidly solidify, thus quench. Also along the margin of dykes, a chilled margin is commonly observed (although in that case the steep temperature gradient is caused by cool and solid country rock).

Is quenching thus pervasive and able to inhibit any further fluid mechanical interaction of two magmas? We believe not, because in nature different types of quench textures may be observed in enclaves of a single deposit, which are indicative of variable temperature contrasts during petrogenesis. Such a case is the 1100 AD monogenetic eruption of Montaña Reventada in Tenerife, Spain. This composite lavaflow (basanite underneath a phonolite) features a sequence of distinct quench and filament textures indicative of thermal equilibration between mafic and felsic fluid during a brief episode of magma mingling (Wiesmaier et al., 2011). The case of Montaña Reventada demonstrates that decreasing temperature gradients or indeed complete thermal equilibration between two magmas of different composition is possible in nature, even at short timescales. In fact, any outcrop featuring magmatic filament textures (e.g. Perugini et al., 2002) is evidence for the potential of two magmas mixing at temperature contrasts too low for quenching. The formation of quench textures has thus to be regarded as a distinct set of problems to the experimental set-up of this study, the purpose of which was to investigate the potential for bubble mixing in the highly viscous but fluid regime.

4.5 Relevance for natural scenarios

The dynamics of bubble mixing can be best appreciated by considering end-member scenarios. These end-member cases are unrealistic, but allow gleaning information on bubble mixing. Two end-member cases can be conceived when conditions are favourable, that is when temperature contrast is low (no quenching) and when a free gas phase is available in the lower magmatic fluid. In one end-member case, all bubbles penetrate the upper rhyolite at distinct loci and no secondary bubbles pass through any filament. This implies the generation of a new filament with every rising bubble. Each filament equilibrates progressively as single-pulse filament into the surrounding rhyo-

SED
7, 1469–1515, 2015

lite. When assuming magmatic temperatures and the associated diffusive velocities, the efficiency of producing a coherent body of hybrid magma then only depends on the number of bubbles rising from the basalt. Progressively, pristine rhyolite will be "filled" with hybrid filaments. This end-member case is thus illustrative, as it shows that after a certain point, new bubbles will have no other option than passing through already hybridized material. The notion of second generation bubbles that exploit previously existing filaments is therefore a necessity. Furthermore, the establishment of a hybridised horizon between basalt and rhyolite also implies that filaments from further bubble ascent will penetrate farther upward into the rhyolite than before.

The other end-member case would be hybridization of a rhyolite by one single filament through which all bubbles must pass. This single filament would be growing in diameter due to the additional mafic magma advected with every rising bubble. Considering a conservative frequency of bubbles of 1 per minute, the filament would be replenished quasi-constantly, therefore leading to a constantly mafic composition inside the filament. At magmatic temperature, however, this filament also equilibrates simultaneously with its surroundings, so a constant flux of ions to and from the filament will, albeit slowly, progressively hybridize the rhyolite, whilst the centre of the filament remains at the most mafic composition due to constant replenishment by new bubbles. Importantly, however, also filament will grow laterally with time by addition of mafic magma from within the filament. This end-member case illustrates that multi-pulse filaments continue to equilibrate with their surroundings despite the possibility of replenishment of the filament to more mafic composition. This continuity of diffusion is inherent to all scenarios of magma mixing, once a compositional gradient is established, diffusion will begin to equilibrate the activities.

The process of bubble mixing has not been observed in nature in isolated form so far. This may partly be because bubbles have not been widely considered up to now as mixing agent. We are able, however, to not only present several lines of deductive or indirect evidence pointing to the role of bubble ascent during the magmatic stage, but also first direct natural evidence. First of all, theoretical deductions (Stokes' law) show

SED
7, 1469–1515, 2015

a linear relation between viscosity and density contrast. Indirect evidence is provided by some natural case studies. Anderson et al. (1989) detected an inverse correlation of H_2O and CO_2 in glass inclusions and quartz phenocrysts throughout the stratigraphy of the Bishop Tuff, USA. Their interpretation offered two possibilities, (a) a closed-system crystallisation to produce large volumes of rhyolitic magma at elevated gas contents and not detected "lost" crystals, or (b) a rise of CO_2 bubbles into the rhyolitic magma from below. In the light of the current understanding of closed vs. open system differentiation, it seems unlikely that the Bishop Tuff ($\sim 650\,km^3$) may be derived from closed system fractionation alone and additionally lose a large percentage of its phenocrysts. An in-depth discussion of open vs. closed systems is out of the scope of this text, but heat of magma and latent heat released during crystallisation of a large volume of magma should have enough impact on country rock to be detectable in the final rock (cf. Reiners et al., 1995; Wiesmaier et al., 2012). In turn, an explanation of rising bubbles of CO_2 into rhyolitic magma is physically conceivable as demonstrated in this study. Moreover, this would be consistent with evidence for pre-eruptive recharge of the Bishop magmatic system (Wark et al., 2007), as mafic recharge would be the most common source of CO_2.

The Licán mafic ignimbrite, erupted from Villarica volcano, Chile, was potentially affected by a free volatile phase as well. In this otherwise homogeneous basaltic andesite, Lohmar et al. (2012) observed two distinct crystal populations with stark disequilibrium textures and overgrowth rims. Mineralogical data and thermodynamic modelling indicated an increase of $\sim 200\,^{\circ}C$ during petrogenesis, interpreted as significant mafic recharge and thermal equilibration. This in combination with the high vesicularity of 53 vol% (uncommon in pre- and post-Licán deposits) suggests that free H_2O bubbles may have contributed to either thermal or compositional equilibration, or indeed both.

Finally, direct evidence is forwarded by samples from Axial seamount. There variability in the MgO content of melt inclusions has been detected (Helo et al., 2011), indicating the general potential for mixing of mafic magma of different composition. Backscattered electron images of samples from Axial seamount show filaments of light

SED
7, 1469–1515, 2015

material attached to vesicles (Fig. 9). These filament show reduced Si and Na contents together with increased Fe, Ca and Mg contents compared to the surrounding basaltic glass (McIntosh, personal communication, 2015). These filaments were probably preserved by rapid quenching of the glass, as otherwise diffusional equilibration at temperatures and viscosities relevant to basaltic systems would act too fast. We question whether this could be the first documented occurrence of bubble advection in natural volcanic material.

In summary, the roles of bubbles in igneous petrogenesis may have been underestimated up to now. While effects of bubbles on the rheology of silicate are currently being researched, their fluid dynamic influence on the mechanic stirring of magma (mingling) has been demonstrated experimentally here.

5 Conclusions

We conducted magma mixing experiments in which bubbles originating from a deep mafic melt intruded into a shallow felsic melt. The results show that bubble ascent provides an efficient mechanism for hybridisation of contrasting melt compositions (in addition to Rayleigh–Taylor instabilities or convection inside a magma reservoir). The combination of tomographic and compositional evidence employed here has identified magma mixing induced by bubble advection. Multiple bubbles were allowed to rise from basalt to rhyolite and later bubbles ascending exploited previously generated vertical filaments as pathway for faster ascent.

Individual filaments were found to be overprinted by passage of multiple bubbles, where each of the bubbles advected additional pulses of mafic material into the same filament. So far, magmatic filaments were tacitly assumed to be only of single pulse origin, as conventional mechanisms of magma mingling (which stretch and fold magma) render replenishment of filaments unlikely. Thus, replenishment of magmatic filaments is probably specific to bubble advection (or particle-based advection, cf. Manga and Stone, 1995).

SED
7, 1469–1515, 2015

The multiple-pulse character of individual filaments has two main implications:

1. Analytical transects of bell-shape across magma mixing filaments may not only be the result of single, but also multiple pulses of mafic material. Multiple episodes of replenishment may have occurred in individual filaments, when a free gas phase was involved in their formation.

2. Because bubble-injection driven homogenisation creates low-viscosity chimneys that facilitate the subsequent passage of more bubbles, the rate of mixing likely accelerates through time so long as a free gas phase is readily available. Acceleration proceeds until the vertical filaments reach the most mafic composition (lowest viscosity) available in a given setting.

We show a new method for distinction of single- from multi-pulse filaments. Based on in-situ compositional data, correlation of concentration variance with filament thickness allows distinguishing whether a set of filaments formed conventionally by single pulse or multiple pulses of replenishment.

We propose that magma mixing induced by bubble advection may be a significant process in nature and may enhance the extent of mixing. Experimentally, this process has now been demonstrated to function under extremely high viscosity contrast. Samples from Axial seamount show evidence for bubble mixing in nature. The smaller viscosity contrasts pertaining within such a mainly basaltic system will facilitate this process further.

Acknowledgements. We are greatly indebted to Iona McIntosh for sourcing the information on the samples from Axial seamount. Fabian Wadsworth helped with the calculation of heating rates. Funding for this project was provided by ICDP-DFG project number CA 905/1-1 and HE 4565/2-1, as well as DFG projects DI 431/31-1 and Di 431/31-2. We wish to acknowledge the European Research Council for the Starting Grant SLiM (no. 306488) awarded to Y. Lavallée, Consolidator Grant CHRONOS (no. 612776) to D. Perugini and Advanced grant EVOKES (no. 247076) to D. B. Dingwell.

SED
7, 1469–1515, 2015

References

Anderson, A. T., Newman, S., Williams, S. N., Druitt, T. H., Skirius, C., and Stolper, E.: H_2O, CO_2, Cl, and gas in Plinian and ash-flow Bishop rhyolite, Geology, 17, 221–225, doi:10.1130/0091-7613(1989)017<0221:hoccag>2.3.co;2, 1989.

Bagdassarov, N., Dorfman, A., and Dingwell, D. B.: Effect of alkalis, phosphorus, and water on the surface tension of haplogranite melt, Am. Mineral., 85, 33–40, 2000.

Blake, S. and Campbell, I. H.: The dynamics of magma-mixing during flow in volcanic conduits, Contrib. Mineral. Petrol., 94, 72–81, 1986c.

Bonnichsen, B.: The Bruneau–Jarbidge Eruptive Center, Southwestern Idaho, in: Cenozoic Geology of Idaho, edited by: Bonnichsen, B. and Breckenridge, R. M., Idaho Bureau of Mines and Geology Bulletin, 237–254, 1982.

Cathey, H. E. and Nash, B. P.: Pyroxene thermometry of rhyolite lavas of the Bruneau–Jarbidge eruptive center, Central Snake River Plain, J. Volcanol. Geotherm. Res., 188, 173–185, doi:10.1016/j.jvolgeores.2009.05.024, 2009.

Chevrel, M. O., Cimarelli, C., deBiasi, L., Hanson, J., Lavallée, Y., Arzilli, F., and Dingwell, D. B.: Viscosity measurements of crystallizing andesite from Tungurahua volcano (Ecuador), Geochem. Geophys. Geosyst., 16, 870–889, doi:10.1002/2014GC005661, 2015.

Clift, R., Grace, J., and Weber, M. E.: Bubbles, Drops, and Particles, Dover Pubn Inc., 381 pp., 2005.

Coombs, M. L., Eichelberger, J. C., and Rutherford, M. J.: Experimental and textural constraints on mafic enclave formation in volcanic rocks, J. Volcanol. Geoth. Res., 119, 125–144, 2003.

De Campos, C. P., Ertel-Ingrisch, W., Perugini, D., Dingwell, D. B., and Poli, G.: Chaotic mixing in the system earth: mixing granitic and basaltic liquids, in: Chaotic Systems: Theory and Application, edited by: Skiadas, C. H. and Dimotilakis, I., Int. Publ. Com., 51–58, 2010.

De Campos, C., Perugini, D., Ertel-Ingrisch, W., Dingwell, D., and Poli, G.: Enhancement of magma mixing efficiency by chaotic dynamics: an experimental study, Contrib. Mineral. Petr., 161, 863–881, doi:10.1007/s00410-010-0569-0, 2011.

Dingwell, D. B.: Viscosity-temperature relationships in the system $Na_2Si_2O_5$-$Na_4Al_2O_5$, Geochim. Cosmochim. Ac., 50, 1261–1265, doi:10.1016/0016-7037(86)90409-6, 1986.

Dingwell, D. B.: Effects of structural relaxation on cationic tracer diffusion in silicate melts, Chem. Geol., 82, 209–216, doi:10.1016/0009-2541(90)90082-i, 1990.

SED
7, 1469–1515, 2015

Eichelberger, J. C.: Vesiculation of mafic magma during replenishment of silicic magma reservoirs, Nature, 288, 446–450, 1980.
Freda, C., Gaeta, M., Misiti, V., Mollo, S., Dolfi, D., and Scarlato, P.: Magma-carbonate interaction: an experimental study on ultrapotassic rocks from Alban Hills (Central Italy), Lithos, 101, 397–415, doi:10.1016/j.lithos.2007.08.008, 2008.
Giordano, D., Russell, J. K., and Dingwell, D. B.: Viscosity of magmatic liquids: a model, Earth Planet. Sc. Lett., 271, 123–134, 2008.
Helo, C., Longpre, M.-A., Shimizu, N., Clague, D. A., and Stix, J.: Explosive eruptions at mid-ocean ridges driven by CO_2-rich magmas, Nature Geosci, advance online publication, available at: http://www.nature.com/ngeo/journal/vaop/ncurrent/abs/ngeo1104.html#supplementary-information, 2011.
Huppert, H. E. and Turner, J. S.: Double-diffusive convection, J. Fluid Mech., 106, 299–329, doi:10.1017/S0022112081001614, 1981.
Huppert, H. E., Sparks, R. S. J., and Turner, J. S.: Laboratory investigations of viscous effects in replenished magma chambers, Earth Planet. Sc. Lett., 65, 377–381, 1983.
Huppert, H. E., Stephen, R., Sparks, J., and Turner, J. S.: Some effects of viscosity on the dynamics of replenished magma chambers, J. Geophys. Res., 89, 6857–6877, doi:10.1029/JB089iB08p06857, 1984.
Izbekov, P. E., Eichelberger, J. C., and Ivanov, B. V.: The 1996 eruption of Karymsky Volcano, Kamchatka: historical record of basaltic replenishment of an andesite reservoir, J. Petrol., 45, 2325–2345, 2004.
Jochum, K. P., Dingwell, D. B., Rocholl, A., Stoll, B., Hofmann, A. W., Becker, S., Besmehn, A., Bessette, D., Dietze, H. J., Dulski, P., Erzinger, J., Hellebrand, E., Hoppe, P., Horn, I., Janssens, K., Jenner, G. A., Klein, M., McDonough, W. F., Maetz, M., Mezger, K., Munker, C., Nikogosian, I. K., Pickhardt, C., Raczek, I., Rhede, D., Seufert, H. M., Simakin, S. G., Sobolev, A. V., Spettel, B., Straub, S., Vincze, L., Wallianos, A., Weckwerth, G., Weyer, S., Wolf, D., and Zimmer, M.: The preparation and preliminary characterisation of eight geological MPI-DING reference glasses for in-site microanalysis, Geostandard. Newslett., 24, 87–133, doi:10.1111/j.1751-908X.2000.tb00590.x, 2000.
Kojima, M., Hinch, E. J., and Acrivos, A.: The formation and expansion of a toroidal drop moving in viscous fluid, Phys. Fluids, 27, 19–32, 1984.

SED
7, 1469–1515, 2015

Lacaze, L., Guenoun, P., Beysens, D., Delsanti, M., Petitjeans, P., and Kurowski, P.: Transient surface tension in miscible liquids, Phys. Rev. E, 82, 041606, doi:10.1103/PhysRevE.82.041606, 2010.
Lohmar, S., Parada, M., Gutiérrez, F., Robin, C., and Gerbe, M. C.: Mineralogical and numerical approaches to establish the pre-eruptive conditions of the mafic Licán Ignimbrite, Villarrica Volcano (Chilean Southern Andes), J. Volcanol. Geoth. Res., 235–236, 55–69, doi:10.1016/j.jvolgeores.2012.05.006, 2012.
Manga, M. and Stone, H. A.: Low Reynolds number motion of bubbles, drops and rigid spheres through fluid–fluid interfaces, J. Fluid Mech., 287, 279–298, doi:10.1017/S0022112095000954, 1995.
Misiti, V., Vetere, F., Mangiacapra, A., Behrens, H., Cavallo, A., Scarlato, P., and Dingwell, D. B.: Viscosity of high-K basalt from the 5th April 2003 Stromboli paroxysmal explosion, Chem. Geol., 260, 278–285, doi:10.1016/j.chemgeo.2008.12.023, 2009.
Mollo, S., Vinciguerra, S., Iezzi, G., Iarocci, A., Scarlato, P., Heap, M. J., and Dingwell, D. B.: Volcanic edifice weakening via devolatilization reactions, Geophys. J. Int., 186, 1073–1077, doi:10.1111/j.1365-246X.2011.05097.x, 2011.
Morgavi, D., Perugini, D., De Campos, C. P., Ertel-Ingrisch, W., and Dingwell, D. B.: Time evolution of chemical exchanges during mixing of rhyolitic and basaltic melts, Contrib. Mineral. Petr., 166, 615–638, doi:10.1007/s00410-013-0894-1, 2013a.
Morgavi, D., Perugini, D., De Campos, C. P., Ertel-Ingrisch, W., and Dingwell, D. B.: Morphochemistry of patterns produced by mixing of rhyolitic and basaltic melts, J. Volcanol. Geoth. Res., 253, 87–96, doi:10.1016/j.jvolgeores.2012.12.007, 2013b.
Morgavi, D., Perugini, D., De Campos, C. P., Ertl-Ingrisch, W., Lavallée, Y., Morgan, L., and Dingwell, D. B.: Interactions between rhyolitic and basaltic melts unraveled by chaotic mixing experiments, Chem. Geol., 346, 199–212, doi:10.1016/j.chemgeo.2012.10.003, 2013.
Pallister, J. S., Hoblitt, R. P., and Reyes, A. G.: A basalt trigger for the 1991 eruptions of Pinatubo volcano?, Nature, 356, 426–428, 1992.
Perugini, D. and Poli, G.: Chaotic dynamics and fractals in magmatic interaction processes: a different approach to the interpretation of mafic microgranular enclaves, Earth Planet. Sc. Lett., 175, 93–103, doi:10.1016/S0012-821X(99)00282-4, 2000.
Perugini, D., Poli, G., and Gatta, G. D.: Analysis and simulation of magma mixing processes in 3D, Lithos, 65, 313–330, 2002.

SED
7, 1469–1515, 2015

Perugini, D., Poli, G., and Mazzuoli, R.: Chaotic advection, fractals and diffusion during mixing of magmas: evidence from lava flows, J. Volcanol. Geoth. Res., 124, 255–279, 2003.
Perugini, D. and Poli, G.: Analysis and numerical simulation of chaotic advection and chemical diffusion during magma mixing: petrological implications, Lithos, 78, 43–66, 2004.
Perugini, D., De Campos, C. P., Ertel-Ingrisch, W., and Dingwell, D. B.: The space and time complexity of chaotic mixing of silicate melts: implications for igneous petrology, Lithos, 155, 326–340, doi:10.1016/j.lithos.2012.09.010, 2012.
Perugini, D., De Campos, C. P., Dingwell, D. B., and Dorfman, A.: Relaxation of concentration variance: a new tool to measure chemical element mobility during mixing of magmas, Chem. Geol., 335, 8–23, doi:10.1016/j.chemgeo.2012.10.050, 2013.
Pouchou, J. L. and Pichoir, F.: Possibilités d'analyse en profondeur à la microsonde électronique, Microsc. Spectrosc. Electron., 9, 99–100, 1984. (NOT FOUND!)
Rallison, J. M.: The deformation of small viscous drops and bubbles in shear flows, Annu. Rev. Fluid Mech., 16, 45–46, 1984.
Reiners, P. W., Nelson, B. K., and Ghiorso, M. S.: Assimilation of felsic crust by basaltic magma: thermal limits and extents of crustal contamination of mantle-derived magmas, Geology, 23, 563–566, 1995.
Ruprecht, P., Bergantz, G. W., and Dufek, J.: Modeling of gas-driven magmatic overturn: tracking of phenocryst dispersal and gathering during magma mixing, Geochem. Geophy. Geosy., 9, Q07017, doi:10.1029/2008GC002022, 2008.
Sánchez Mirón, A., Cerón García, M. C., García Camacho, F., Molina Grima, E., and Chisti, Y.: Mixing in bubble column and airlift reactors, Chem. Eng. Res. Des., 82, 1367–1374, doi:10.1205/cerd.82.10.1367.46742, 2004.
Snyder, D. and Tait, S.: Magma mixing by convective entrainment, Nature, 379, 529–531, 1996.
Tait, S. and Jaupart, C.: Compositional convection in viscous melts, Nature, 338, 571–574, 1989.
Thomas, N., Tait, S., and Koyaguchi, T.: Mixing of stratified liquids by the motion of gas bubbles: application to magma mixing, Earth Planet. Sci. Lett., 115, 161–175, doi:10.1016/0012-821x(93)90220-4, 1993.
Wark, D. A., Hildreth, W., Spear, F. S., Cherniak, D. J., and Watson, E. B.: Pre-eruption recharge of the Bishop magma system, Geology, 35, 235–238, doi:10.1130/g23316a.1, 2007.
Wiesmaier, S., Deegan, F., Troll, V., Carracedo, J., Chadwick, J., and Chew, D.: Magma mixing in the 1100 AD Montaña Reventada composite lava flow, Tenerife, Canary Islands: interaction

SED
7, 1469–1515, 2015

between rift zone and central volcano plumbing systems, Contrib. Mineral. Petr., 162, 651–669, doi:10.1007/s00410-010-0596-x, 2011.

Wiesmaier, S., Troll, V. R., Carracedo, J. C., Ellam, R. M., Bindeman, I., and Wolff, J. A.: Bimodality of lavas in the Teide–Pico Viejo succession in Tenerife – the role of crustal melting in the origin of recent phonolites, J. Petrol., 53, 2465–2495, doi:10.1093/petrology/egs056, 2012.

Wilcox, R. E.: The idea of magma mixing: history of a struggle for acceptance, J. Geol., 107, 421–432, doi:10.1086/314357, 1999.

Woods, A. W. and Cowan, A.: Magma mixing triggered during volcanic eruptions, Earth Planet. Sci. Lett., 288, 132–137, doi:10.1016/j.epsl.2009.09.015, 2009.

Zhang, Y.: Diffusion in Minerals and Melts: theoretical Background, Rev. Mineral. Geochem., 72, 5–59, 2010.

SED
7, 1469–1515, 2015

Table 1. Composition of end-member glasses from the Snake River Plain (data from Morgavi et al., 2013).

[wt%]	SRP Basalt	SRP Rhyolite
SiO_2	48.11	79.16
Al_2O_3	16.19	9.81
TiO_2	1.76	0.23
MgO	7.42	0.12
FeO_{tot}	12.12	1.84
MnO	0.28	0
CaO	11.46	0.83
Na_2O	1.94	3.47
K_2O	0.31	4.53
P_2O_5	0.43	0
Total	100	100

SED
7, 1469–1515, 2015

Table 2. Compilation of measured radii of bubbles suspended in rhyolite glass. Ellipsoid radii r1, r2 and r3 are given, along with normalised radii and sum of normalised radii.

	Ellipsoid radii [voxel]			Normalised radii [dim.less]			
Bubble ID	r1	r2	r3	r1_norm	r2_norm	r3_norm	total
1	16.35	15.94	15.59	0.34	0.33	0.33	1.00
2	19.81	19.65	19.28	0.34	0.33	0.33	1.00
3	14.11	13.79	13.37	0.34	0.33	0.32	0.99
4	10.18	9.42	9.26	0.35	0.33	0.32	1.00
5	14.36	14.06	13.78	0.34	0.33	0.33	1.00
6	6.31	5.79	5.55	0.36	0.33	0.31	1.00
7	8.25	8.04	7.87	0.34	0.33	0.33	1.00
8	9.31	9.17	9.02	0.34	0.33	0.33	1.00

SED
7, 1469–1515, 2015

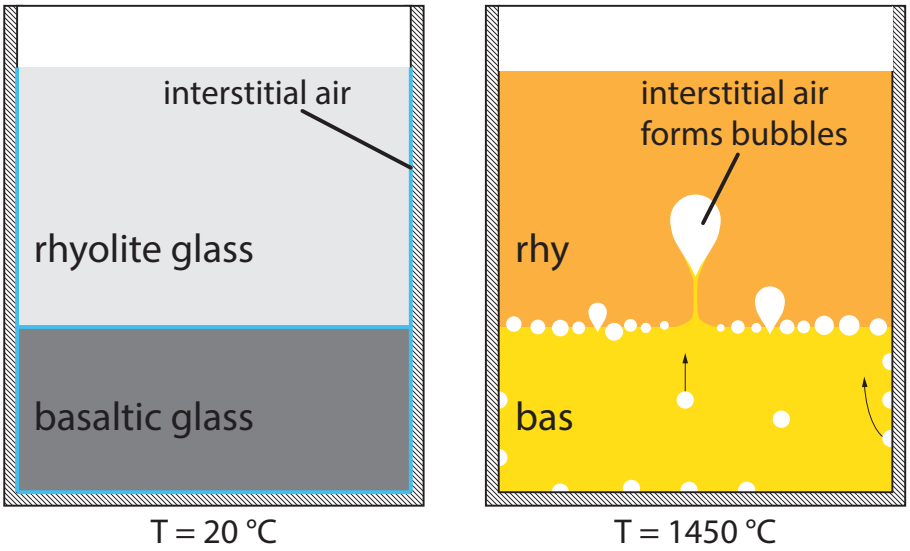

Figure 1. Experimental set-up. **(a)** Glass cyclinders of basalt and rhyolite were placed above each other at room *T* into a Pt-crucible and heated to 1450 ˚C. **(b)** Air trapped in-between the glass cylinders expands and forms bubbles upon heating.

SED
7, 1469–1515, 2015

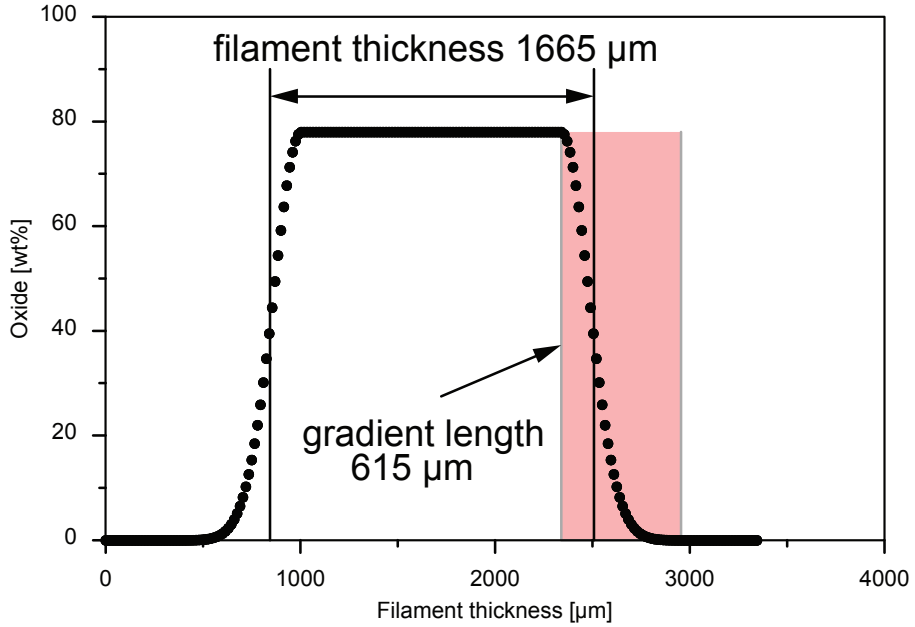

Figure 2. Modelled compositional profile after the thin-source problem (e.g., Zhang, 2010). Filament thickness is determined by selecting the intermediate points of each profile. Gradient length denotes the part of the compositional profile, in which the composition shows variations.

SED
7, 1469–1515, 2015

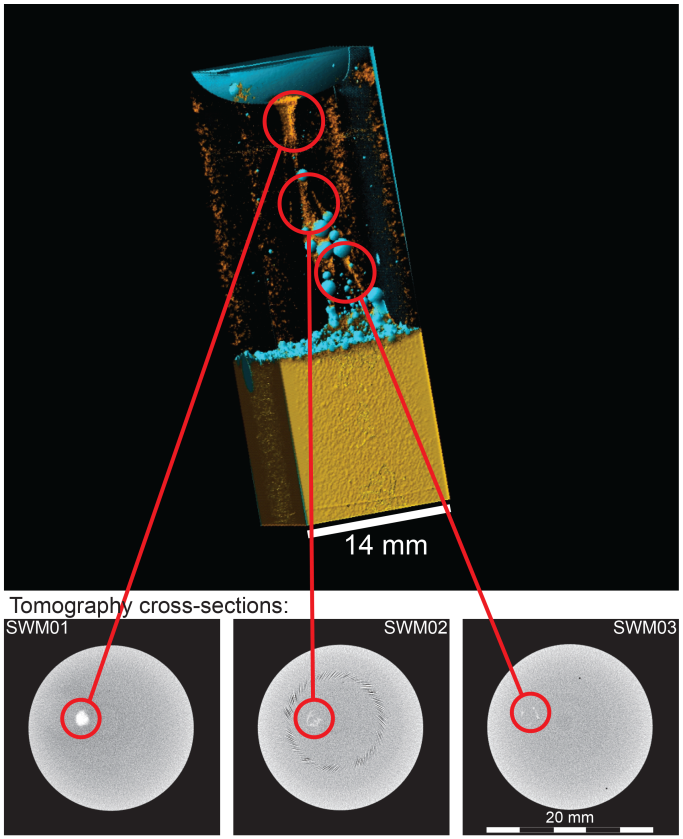

Figure 3. 3-D representation of the experimental charge. The lower yellow layer is basaltic glass, whereas the upper rhyolitic layer has been rendered transparent. Hybrid material was rendered orange as a result of differing attenuation behaviour. The experimental charge has subsequently been sliced along three horizons for cross-sections which were measured in-situ by EMP.

SED
7, 1469–1515, 2015

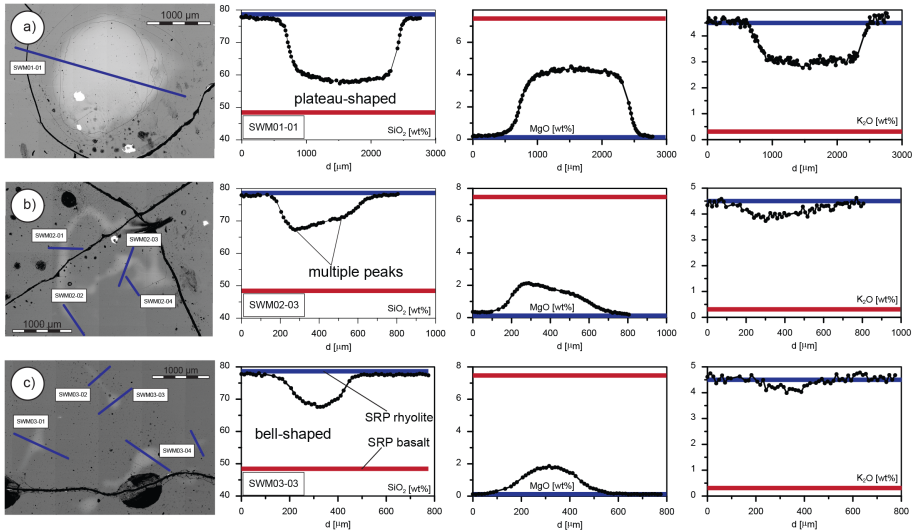

Figure 4. Backscattered electron images of slices of experimental glass and exemplary major element concentration profiles across the hybrid plume structures. Blue and red lines indicate the initial compositions of the end-members basalt and rhyolite. Note that in all EMP transects, the initial composition of the basalt has been obliterated, i.e. the plume tail has been pervasively hybridised.

SED
7, 1469–1515, 2015

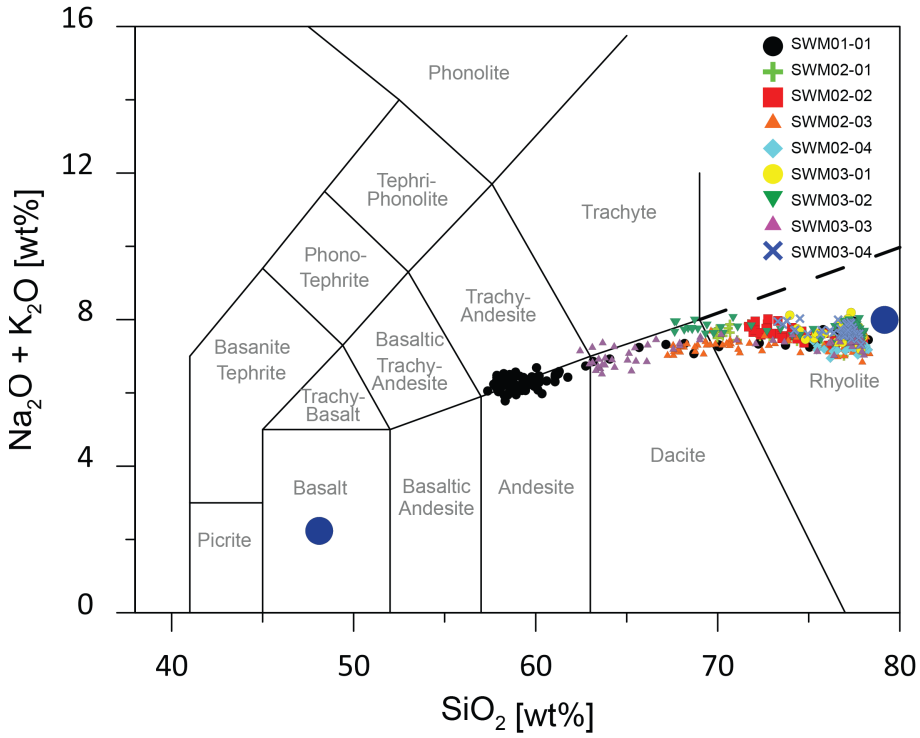

Figure 5. TAS plot of end-member compositions and hybrid compositions produced during the bubble advection experiment. Data normalised to 100 % totals. Blue and red circles denote the end-member compositions of Snake River Basalt and Rhyolite.

SED
7, 1469–1515, 2015

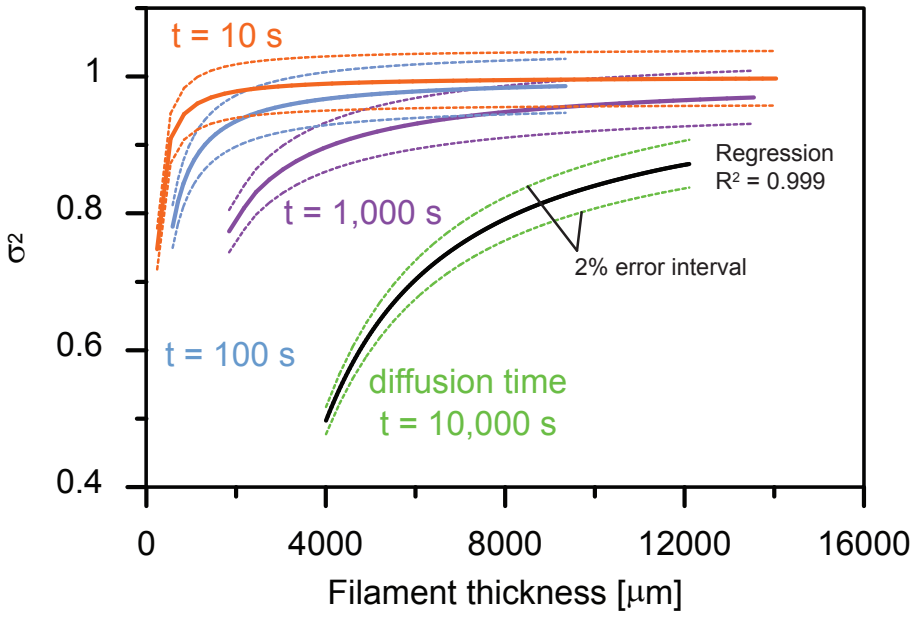

Figure 6. Modelled viscosity of filament compositions after Giordano et al. (2008), two panels for clarity. The calculation of viscosity contrast for each filament is indicated by the arrow.

SED
7, 1469–1515, 2015

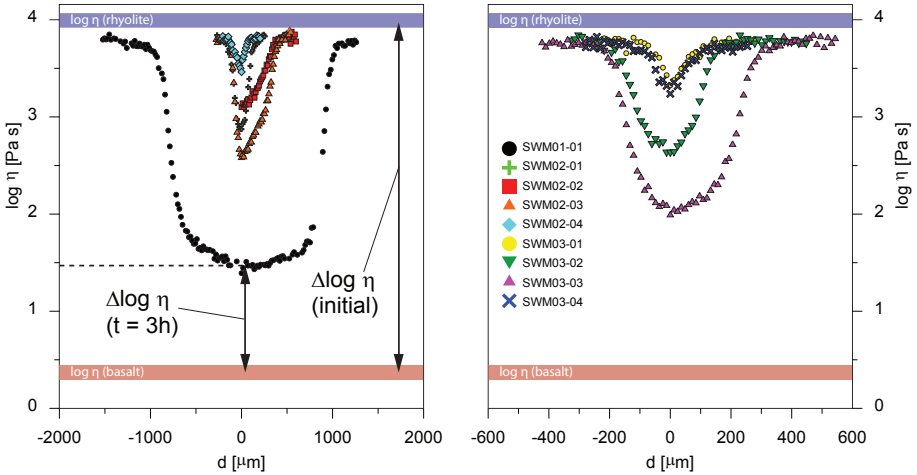

Figure 7. Ideal behaviour of concentration variance depending on filament thickness. Each data point represents the concentration variance of an entire diffusion profile correlated with the filament thickness of that profile. Four curves were calculated for different diffusion times, which are indicated in the graph. Each curve shows a 2 % error interval (dotted lines).

SED
7, 1469–1515, 2015

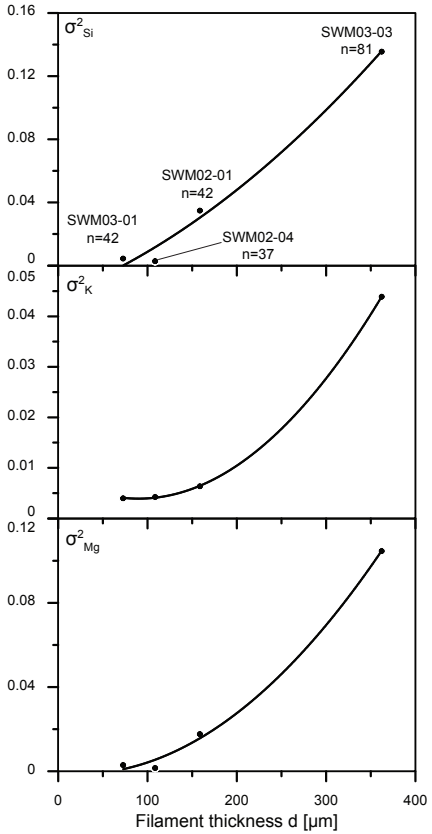

Figure 8. Concentration variance of experimental filaments vs. filament thickness for experimental filaments that yielded compositional profiles of bell-shape. The best-fit regression curves for the experimental filaments are polynomial and yield high R^2 values. The four data points represent four analytical transects of altogether 202 EMP data points.

SED
7, 1469–1515, 2015

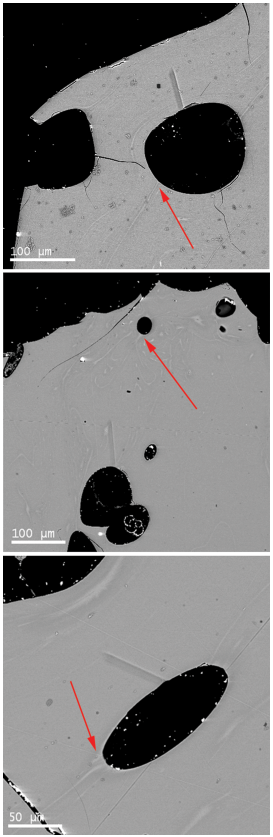

Figure 9. Backscattered electron images of basaltic glass from Axial seamount (McIntosh, personal communication, 2015). Red arrows indicate filaments of more mafic composition than surrounding glass, attached to vesicles.

SED
7, 1469–1515, 2015